The Astrophysical Journal, 849:36 (15pp), 2017 November 1 https://doi.org/10.3847/1538-4357/aa8ea2

The Flaring Activity of M Dwarfs in the Kepler Field

Huiqin Yang[1,2], Jifeng Liu[1,2], Qing Gao[1], Xuan Fang[3,4,7], Jincheng Guo[5,8], Yong Zhang[6], Yonghui Hou[6], Yuefei Wang[6], and Zihuang Cao[1]
[1] Key Laboratory of Optical Astronomy, National Astronomical Observatories, Chinese Academy of Sciences, Beijing 100012, China; yhq@nao.cas.cn
[2] University of Chinese Academy of Sciences, Beijing 100049, China
[3] Laboratory for Space Research, University of Hong Kong, Pokfulam, Hong Kong, China
[4] Department of Earth Sciences, University of Hong Kong, Pokfulam, Hong Kong, China
[5] Department of Astronomy, Peking University, Beijing 100871, China
[6] Nanjing Institute of Astronomical Optics & Technology, National Astronomical Observatories, Chinese Academy of Sciences, Nanjing 210042, China
Received 2017 July 3; revised 2017 September 20; accepted 2017 September 20; published 2017 October 27

Abstract

Flare events are mainly due to magnetic reconnection and thus are indicative of stellar activity. The *Kepler Space Observatory* records numerous stellar activities with unprecedented high photometric precision in flux measurements. It is perfectly suitable for carrying out a statistical study of flares. Here we present 540 M dwarfs with flare events discovered using *Kepler* long-cadence data. The normalized flare energy, as defined by the ratio to bolometric stellar luminosity, $L_{\rm flare}/L_{\rm bol}$, is used to indicate the flare activity. We find that, similar to the X-ray luminosity relation, the $L_{\rm flare}/L_{\rm bol}$ versus $P_{\rm rot}$ relation can also be described with three phases, supersaturation, saturation, and exponential decay, corresponding to an ultra-short period, a short period, and a long period. The flare activity and the number fraction of flaring stars in M dwarfs rise steeply near M4, which is consistent with the prediction of a turbulent dynamo. The size of starspots are positively correlated with flare activity. The $L_{\rm flare}/L_{\rm bol}$ ratio has a power-law dependence on $L_{\rm H\alpha}/L_{\rm bol}$, a parameter indicative of stellar chromosphere activity. According to this relation, a small enhancement in chromosphere activity may cause a huge rise in flare energy, which suggests that superflares or hyperflares may not need an extra excitation mechanism. Through a comparison study, we suggest that flare activity is a more suitable indicator for stellar activity, especially in the boundary region. However, contrary to what is expected, some M dwarfs with strong flares do not show any light variation caused by starspots. Follow-up observations are needed to investigate this problem.

Key words: stars: activity – stars: flare – stars: late-type – stars: statistics – starspots

Supporting material: machine-readable tables

1. Introduction

Flares are intense energy outburst events on the stellar surface lasting for hours. The rapid rise of the flux has been observed in a wide range in wavelengths from radio to gamma-ray (Benz & Güdel 2010). On our Sun, it is well known that flares are energy releases of the magnetic field reconnections in the outer atmosphere with energies ranging from 10^{29} to 10^{32} erg. However, Maehara et al. (2012) found that, on other solar-like stars, the released energy could exceed 1000 times that on the Sun. The cooler stars such as K and M dwarfs also show similar, surprisingly energetic flares (Kowalski et al. 2013). Superflares on the most active stars, M dwarfs, are common and have been widely studied (e.g., Walkowicz et al. 2011; Hawley et al. 2014; Chang et al. 2017). During these flare events, the total energy could be more than 10^{34} erg, accompanied by chromospheric and coronal emission lines. For those super energy release events, other explanations with respect to the flare mechanism are also possible, such as disruption of the interconnecting field lines for the RS CVn binary (Simon et al. 1980) and the enhanced dynamo action by tidal interaction in the star–planets system (Rubenstein & Schaefer 2000; Ip et al. 2004). Flares, as well as emission line variations play an important role in stellar activity, and thus it is interesting to study the relation between light variation and spectral features. Kowalski et al. (2010) observed enhanced continuum and Balmer emission lines when the flare occurs and fitted the continuum well with a $T_* \sim 10{,}000$ K blackbody radiation model. Similar results have been found in several works (e.g., Mochnacki & Zirin 1980; Kretzschmar 2011).

The most important factor responsible for stellar activity is a magnetic field (e.g., Parker 1979), which can leave clues in the corona, chromosphere, and photosphere. Previous studies based on the Hα and Ca II emission lines as well as the coronal X-ray emission found that the stellar activity had a close relation with rotational period and convective envelope depth (e.g., Reiners 2012). Moreover, the saturation regime is presented in the relationship between the indicator of stellar activity and the period or Rossby number (Pizzolato et al. 2003; Wright et al. 2011), although its nature is under debate.

Flares, as the result of magnetic reconnection, could also be indicative of stellar activity. For active stars, flares are very common and their statistical properties are a good proxy for stellar activity. Such studies have been supported by a wealth of data from the *Kepler* program (Borucki et al. 2010). The *Kepler* satellite is designed to obtain high-precision and long-baseline light curves of numerous stars. It has ushered in a new era of stellar photometric investigation, enabling light-curve

[7] Visiting Astronomer, Key Laboratory of Optical Astronomy, National Astronomical Observatories, Chinese Academy of Sciences, Beijing 100012, China.
[8] LAMOST Fellow.

analysis with unprecedented precision: about 0.1 mmag for a star of 12 mag (Koch et al. 2010). Since *Kepler* monitors many stars simultaneously, the mission has yielded light curves for 200,000 stars with over four years of continuous observations. These light curves provide unique opportunities to study stellar activities such as statistical properties of the stellar flares, and the periodic variations that can be attributed to starspots rotating across the visible hemisphere.

Recent research (e.g., Maehara et al. 2012; Shibayama et al. 2013) used *Kepler* data to investigate the G-type star superflares and found that the occurrence rate of flares satisfied a power-law relation, i.e., $dN/dE \sim E^{-\alpha}$ with $\alpha \sim 2$. The flare energy ranges from $\sim 10^{31}$ to 10^{36} erg, and the periodic light curve suggested the existence of starspots. Hawley et al. (2014) obtained a similar α index using five M dwarfs and reported the strong correlation between flare energy, amplitude, duration, and decay time.

The mechanism to generate and maintain the magnetic field, i.e., stellar dynamo, has been extensively discussed. The early M dwarfs, which retain a radiative core, presumably have a solar-type dynamo, while the mid-M dwarfs, which are fully convective, have a turbulent dynamo (e.g., Wright et al. 2011). The two dynamos result in a lot of differences in observations. For example, stronger, and more stable poloidal magnetic fields are reported in the turbulent dynamo while the solar-type dynamo exhibits a weak, toroidal field with a large-scale structure (Donati et al. 2008; Morin et al. 2008). The large-scale fields contribute at most 15% of the total magnetic flux (Reiners & Basri 2009). As a result, it is believed that as the stellar structure becomes fully convective near M4, the level of stellar activity will increase steeply. On the other hand, the inactive stars without observable Hα emission activity exhibit active flares (Hilton 2011), and the hot A-type stars that are expected to have no convection envelopes are also reported to present flares (Balona 2012). These observations imply possibly different mechanisms for stellar flares.

As many flares in late-type stars are found in the *Kepler* data, it is interesting to study the flare mechanisms and their possible relation with other indicators of stellar activity. In this work, we investigate the statistical properties of flares on the most active stars, M-type dwarfs, and try to discern the different mechanism of flares. In Section 2, we provide light curves and spectra and describe the method of analysis. In Section 3, the main results of statistical analysis are presented and discussed. We then elucidate implications for the possible physical mechanism of flares in Section 4 and present our summary in Section 5.

2. Data and Analysis Method

2.1. The Kepler and LAMOST Data

The *Kepler* satellite carries an optical telescope with a 95 cm aperture and 105 deg^2 field of view (about 12° diameter), which is in Cygnus, Lyra, and Draco. Since it aimed to search for exoplanets by finding planetary transit events, *Kepler* is designed to obtain unprecedented precision and continuous white light curves. The precision for the bright targets ($V = 9$–10) approaches 10 ppm and 100 ppm even for faint targets ($V = 13$–14). Our work is based on the entire *Kepler* mission data set (Q1-Q17; 48 months; Data Release 25). It supplies two kinds of time resolution data, which are long-cadence (LC) data with about a thirty-minute sampling interval and short-cadence (SC) data with about one-minute sampling interval. LC data can be used to study flares lasting longer than an hour, while it is not suitable to study shorter flares or the detailed shape of the flares (Balona 2015). However, the profiles of the flares in the SC and LC data are similar. Their durations and energies are in agreement within the errors (Shibayama et al. 2013). Thus LC data grasp the basic properties of flares. SC data is more suitable for the study of stellar flares, but there are only about 4800 sources with SC data, and usually with rather short time coverage (mostly about two months). Because our purpose is to study the statistical properties of the flare energy, and the contribution of the short-lived flares to the energy statistics is small, LC data spanning up to 17 quarters of observation are chosen while SC data will be a valid supplement. *Kepler* provides uncorrected simple aperture photometry (SAP) and pre-search data conditioning (PDC) in which instrumental effects are removed. However, PDC data could also remove some outliers that may be flare peaks, and detrend the long periodic variation caused by starspot rotation, therefore, SAP data are utilized in our research, as is done in Balona (2015) and Davenport (2016).

The physical parameters of most *Kepler* targets such as effective temperatures, surface gravities, and stellar radius have originally been obtained through multi-color photometry, and listed in the Kepler Input Catalog (KIC; Brown et al. 2011). However, their inconsistency with the stellar theory and observations are frequently reported (e.g., Verner et al. 2011; Batalha et al. 2013; Dressing & Charbonneau 2013; Everett et al. 2013), and the continuous revised stellar properties are proposed. These revisions are based on broadband photometry, asteroseismology, spectroscopy, exoplanet transits, and other references. Now it becomes a more reliable catalog (Huber 2014; Huber et al. 2014; Mathur 2016). KIC also gives the position and star numbers for each target, which are used in our study for cross-matching and contamination examination. Given that the aim of this study is to detect flares on M-type dwarfs, we select targets where the temperature $3000\ \mathrm{K} < T < 4000\ \mathrm{K}$ and the surface gravity $\log g > 4.0$. The temperature and surface gravity error bars are, respectively, ± 200 K and ± 0.1, according to Brown et al. (2011). Finally, the number of the selected stars are 4664.

In order to make spectroscopic studies of our targets, we also used the Large Sky Area Multi-Object Fibre Spectroscopic Telescope[9] (LAMOST, Su et al. 1998; Cui et al. 2012) for the observations. LAMOST is a medium aperture (4–6 m) optical telescope designed to mainly carry out spectral surveys of the northern sky stars in the Milky Way, distant galaxies, and QSOs. It well covers the *Kepler* fields considered in our study. The *Kepler*-LAMOST synoptic project was proposed by De Cat et al. (2015) to provide a database for both the study of stellar light variation and spectroscopy. The spectral resolution of LAMOST is $R \sim 1800$ and wavelength coverage is $\sim$3700–9000 Å. A cross-identification between the catalog of LAMOST Data Release 4 (A. Luo et al. 2017, in preparation) and the *Kepler* archive was made with a tolerance of $<3''$ in coordinates. As the Hα line in the spectrum was used in this work, the threshold signal-to-noise ratio (S/N) in the r and i bands is set to be $\gtrsim 10$.

[9] Also named the Guoshoujing Telescope (GSJT). URL http://www.lamost.org.

2.2. Flare Detection

A flare is an intense light -curve variation with rapid rise and relatively slow decay, which can be detected as an outlier against the continuum flux. Based on this character, there are various flare detection algorithms (Walkowicz et al. 2011; Osten et al. 2012; Davenport 2016; Gao et al. 2016), in which the first step is to detrend the light curve, i.e., to remove the continuum flux with an appropriate median filter. Moreover, the flaring stars often have apparent periodic light variations caused by starspots. Most of their periods are given by McQuillan et al. (2014) and Reinhold et al. (2013), and the rest are calculated with the Lomb–Scargle algorithm. In our work, a high-order B spline function (Press 1992) was used to fit the data in each quarter, with an iterative σ-clipping approach applied to remove possible flares before fitting the continuum. The filter width of the fit points is determined to be one-tenth of the rotational period, and we set its upper limit to be one day because of two reasons: (i) according to our statistic records, the duration of flare peaks do not exceed 12 hr (24 points); (ii) if the filter width is large, there could be some instrumental effects and relatively short-period variation in the long-period stars that may be mistaken for flares. If the M dwarfs do not have apparent periods, we set their filter widths to be one day. There are many discontinuities caused by instrumental errors in some quarters such as the well-known discontinuity in Q2 (Coughlin et al. 2016). These inner discontinuities are divided into blocks for fits to avoid the differences in flux (Davenport 2016).

Due to the large data set, the robovetting procedure of flares was applied first. It is known that there are some isolated points either caused by instrumental effects or by cosmic rays. Therefore, in order to distinguish these outliers from real flares, we defined two consecutive points above 3σ in the remaining curve as the beginning of a flare, and the last continuous point higher than 1σ as the end of a flare. Panel (d) of Figure 1 shows an example of auto-searching of the flares. There were three apparent peaks that were not marked as flares, whose details are illustrated in panels (a), (b), and (c), because there was only one point higher than 3σ of the remaining light curve.

After the robovetting procedure, it is necessary to check all the flares by eye. According to the main principle that the flares identified by the robovetter and by eye should be mostly similar, we may fine tune the filter width for some stars and exclude the outliers without the impulsive rise/exponential decay light-curve shape. About 2000 flare candidates with symmetrical profiles (e.g., Figure 1, panel e) were ruled out.

Moreover, Shibayama et al. (2013) pointed out that, if the period is comparable to the timescale of flare duration, it is possible to detrend the flares. This problem is significant in the short-period (<0.5 day) stars because of two reasons: (i) the periodic variation of the light curve is comparable to the durations of some long flares; (ii) the fast rotating M dwarfs often have strong starspots that result in light variations with large amplitudes, and weak flares that may be treated as the quiescent stellar fluxes (i.e., the local continuum) through slightly different fitting. In our view, the best method to identify the flares in those stars is to check by eye. In our samples, there are several flaring M dwarfs with periods shorter than 0.5 day. All the light curves were checked manually.

The manual check mainly emphasized two issues. (i) For the strong flares lasting more than 3 hr, we reconstructed their quiescent fluxes using the neighboring periodic light curves. An example of this is shown in panel (f) of Figure 1. (ii) For the weak flare candidates located in the segments where the quiescent fluxes changed rapidly, we tried to reconstruct the quiescent fluxes using the neighboring data points, and determine the location of the flare through the optimum fit and according to our experiences. As shown in panel (g) of Figure 1, the flare profile largely depends on the continuum fit and it is hard to distinguish whether a small peak is due to a real flare or a starspot. Therefore, we adopted a conservative criteria for the marginal cases.

It should be noted that the flare detection procedure has several stages with heuristic choices that are based on our experiences. Therefore, the resulting flare catalog, are essentially not reproducible.

2.3. Contamination Check

The typical photometric aperture of *Kepler* has a radius of 4–7 pixels (Bryson et al. 2010). It is thus quite common for a given target star to be contaminated by nearby objects, given that some sources are very close to each other on *Kepler*'s CCDs. About 10% of flare candidates are probably untrue due to various reasons (Shibayama et al. 2013; Gao et al. 2016). In order to avoid these false events, we checked for possible contamination following these three steps.

(1) 55 flaring dwarfs with field stars located within 12″ were excluded (Shibayama et al. 2013).

(2) The *Kepler* eclipsing binary catalog (KEB;[10] released on 2016 November 29) includes more than 2800 binary stars. Nine of them were removed from our sample. Admittedly, some sources in the KEB catalog are probably giants, sometimes inflated planets (Faigler et al. 2013). KIC 11548140 has been reported to present a "V" shape when a transit occurs (Batalha et al. 2013). It is flagged as a planet candidate in the NASA Exoplanet Archive[11] (Akeson et al. 2013). It is more likely to be a hot Jupiter that exhibits planet reflection and/or thermal emission (Coughlin et al. 2016). We decided to drop a small number of flaring M dwarfs with planets so that no possible contamination of eclipsing binaries will be introduced into our samples.

(3) The contamination from other stars might cause centroid offset on a pixel image. Here we adopted the approach of Coughlin et al. (2016) to detect centroid offsets of transit signals. This procedure includes the following. (i) A difference/residual image is created by subtracting the quiescent frame (i.e., the image before the flare occurs) from the image with peak flares. (ii) We check whether this residual image contains a discernible star and whether it is dominated by the background noise. This was done by searching for at least three adjacent pixels with emission above a given threshold, which was defined by the noise level of the image. An iterative σ-clipping approach was used to eliminate bright pixels for calculating the background noise (Bryson et al. 2013). (iii) We checked whether the location of the brightest pixels in a residual image coincides with that of the target star. If our objectives were not met in steps (ii) and (iii), the flare candidate would be discarded. About 4700 flare events were removed. Figure 2 shows an example of a contamination check for the event KIC 2300039.

[10] http://keplerebs.villanova.edu/
[11] http://exoplanetarchive.ipac.caltech.edu/

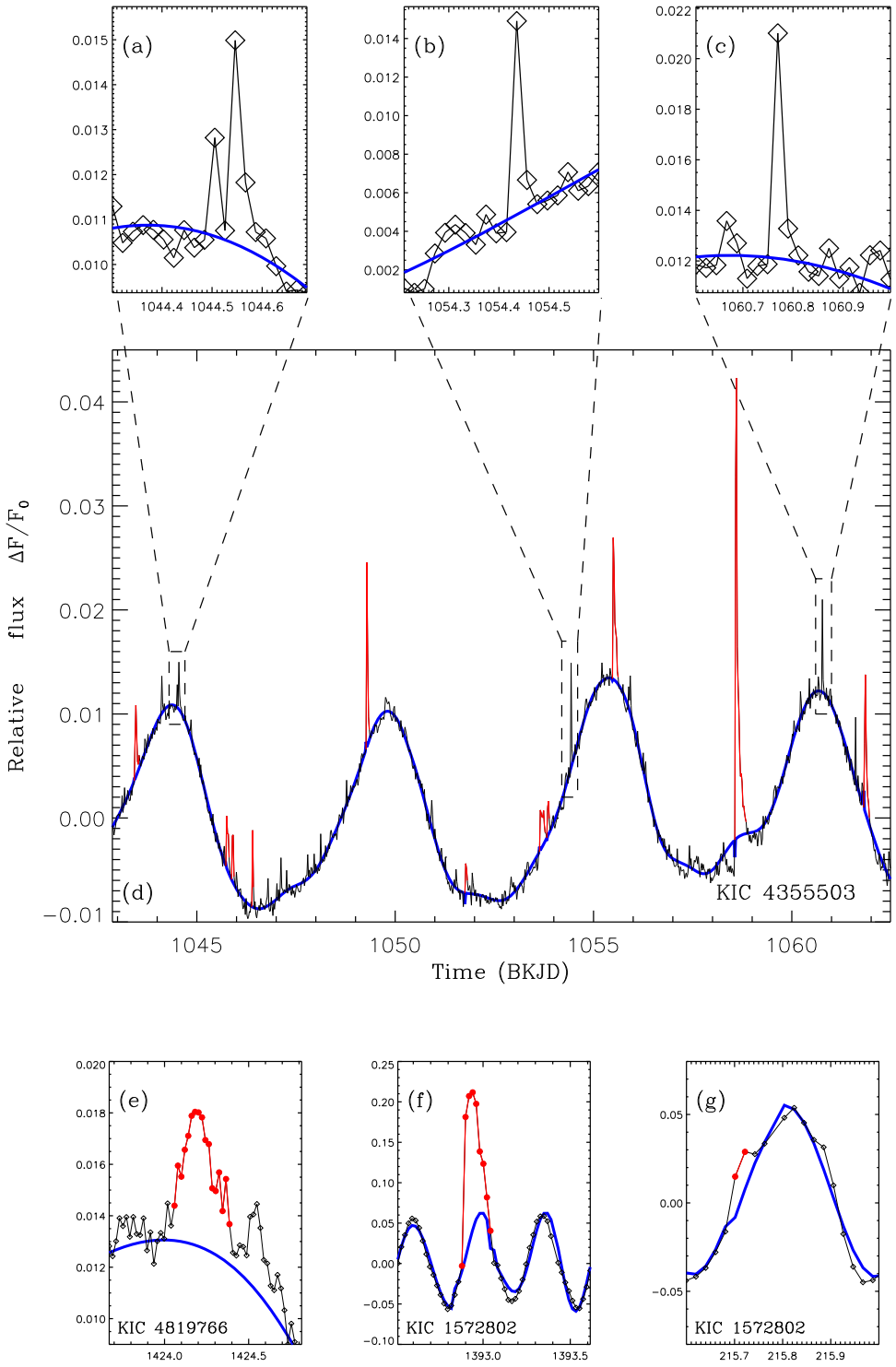

Figure 1. Examples of flare searching. The horizontal axis is the *Kepler* Barycentric Julian Day (BKJD; BJD−2454833) and the vertical axis is the relative flux (see the definition in the text). The black line is the observed stellar flux, the blue line is the continuum fit, and the red line marks the stellar flare. Panel (d) shows a complete section of a light curve to demonstrate the robovetting procedure; in this curve, there are three emission peaks that are not marked as flares, and panels (a), (b), and (c) are the zoom-in of them. The three emission peaks all have only one data point $\sim 3\sigma$ above the local continua. Panel (e) shows a flare candidate with a symmetric profile that was excluded in this study. Panel (f) shows a flare whose duration is a considerable portion of the star's rotation rate. Panel (g) shows the identification and fit of a very weak flare event.

2.4. Energy Estimate

We estimated the flare energy with the method proposed by Shibayama et al. (2013) that utilizes the stellar luminosity and flare amplitude and duration. Mochnacki & Zirin (1980) and Kretzschmar (2011), respectively, found that the white light flare on an M dwarf can be described by a blackbody radiation model with the effective temperature of 9000 K. Therefore, the bolometric flare luminosity $L_{\rm flare}$ can be calculated from the

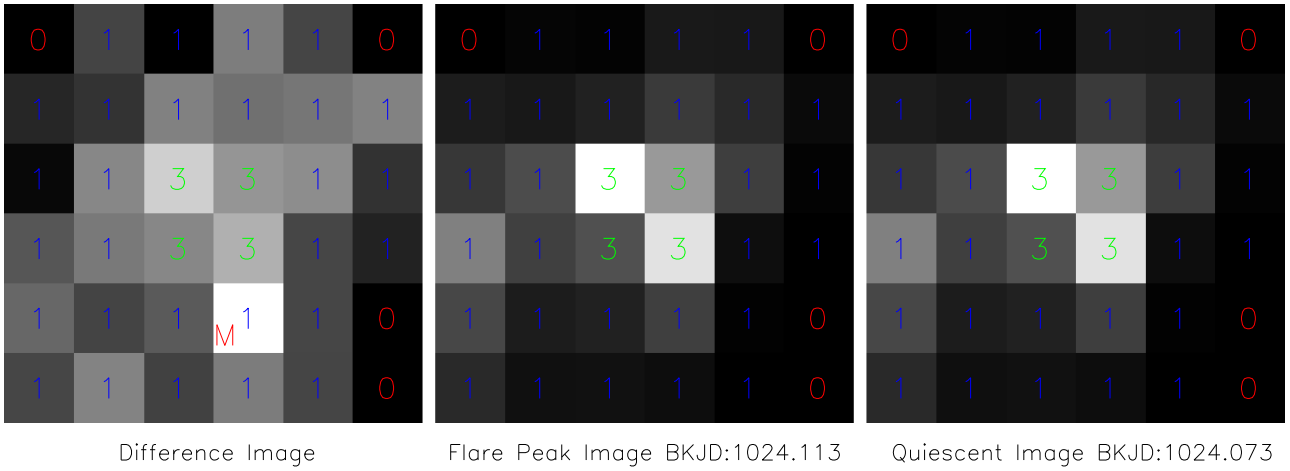

Figure 2. Example of a contamination check for KIC 2300039. The middle panel shows the pixel level data of a flare peak at the time of 1024.113 BKJD, while the right panel shows the image of the same pixels at quiescent status one hour previous. A difference between the two images is shown in the left panel. The number in each pixel means that (1) the pixel was considered for the analysis of light curve, (3) the pixel was in the optimal aperture that represents the location of a star, and (0) the pixel was not used. In the left residual panel, the pixel marked with "M" is not the location of a star and was considered as contamination.

Stefan–Boltzmann law,

$$L_{\rm flare} = \sigma_{\rm SB} T_{\rm flare}^4 A_{\rm flare}, \quad (1)$$

where $\sigma_{\rm SB}$ is the Stefan–Boltzman constant. $T_{\rm flare}$ is the effective temperature assumed to be 9000 K in this study. $A_{\rm flare}$ is the area of the flare, and according to Shibayama et al. (2013), it can be estimated by the ratio of flare luminosity and stellar luminosity using

$$A_{\rm flare} = C_{\rm flare} \pi R^2 \frac{\int R_\lambda B_\lambda(T_{\rm flare}) d\lambda}{\int R_\lambda B_\lambda(T_{\rm eff}) d\lambda}, \quad (2)$$

where R_λ is the *Kepler* response function (Van Cleve & Caldwell 2009), $B_\lambda(T)$ is the Plank function, and R is the stellar radius; $C_{\rm flare}$ is the flare amplitude defined as $C_{\rm flare} = (F_{\rm i} - F_{\rm o})/F_{\rm o}$, where $F_{\rm i}$ is the measured flux sampled at each flare time and $F_{\rm o}$ is the quiescent flux.

$L_{\rm flare}$ can be estimated from Equations (1) and (2). The total bolometric energy of a superflare ($E_{\rm flare}$) is an integral of $L_{\rm flare}$ over the whole duration as shown in the equation:

$$E_{\rm flare} = \int_{\rm flare} L_{\rm flare}(t) dt. \quad (3)$$

It should be noted that Shibayama et al. (2013) estimated the total uncertainty in flare energy to be ±60%.

2.5. Indicator of Stellar Activity

The main purpose of our work is to study flare energy and stellar activity on the M dwarfs using light curves and spectra data. There are some classical indicators of stellar magnetic activity, such as $L_{\rm x}/L_{\rm bol}$ and $L_{\rm H\alpha}/L_{\rm bol}$ (Vilhu 1984; West et al. 2015; Guinan et al. 2016; Suárez Mascareño et al. 2017). In the *Kepler* bandpass, $L_{\rm flare}/L_{\rm K_p}$ was used to characterize each star's flare activity level (Lurie et al. 2015; Davenport 2016). Gao et al. (2016) used the ratio between equivalent width (EW) of the flare and the observational time to measure the binary activity. Since the flare energy depends on stellar energy and luminosity (Balona 2015), we define the flare activity (FA) to be the ratio of total flare energy to total stellar energy emitted during the observations:

$$\mathrm{FA} = \frac{\sum E_{\rm flare}}{\int L_{\rm bol} dt} = \frac{L_{\rm flare}}{L_{\rm bol}}. \quad (4)$$

Here, $\sum E_{\rm flare}$ is the sum of all detectable flare energies during the whole observation; $L_{\rm bol}$ was estimated using the effective temperature and stellar radius given by KIC based on the assumption that the stellar radiation follows a blackbody. This definition is straightforward because it shows the ratio of the flare energy to the total stellar energy. It should be noted that there are many microflares (Shimizu 1995) and nanoflares (Aschwanden et al. 2000) whose energies are much lower than our detection limit, and their total flare energies are difficult to estimate. Hence in our research, the flare activity only represents the superflares that last for more than one hour with the *Kepler* accuracy.

The Hα emission line as well as other indicators like the Ca II lines and X-ray emission, is a well-known proxy for stellar activity (Reiners 2012), which can be measured from the LAMOST spectra. The EW of Hα was estimated in a spectrum by choosing two points at 6550 and 6580 Å to set the continuum level. We checked through all the LAMOST spectra and found that all observed wavelengths of Hα of our targets are well located between these two wavelengths. The EW of Hα was then measured by integrating from 6553 to 6573 Å after flux normalization.

However, EW is not a suitable indicator of stellar activity because the continuum flux is very sensitive to the effective temperature (Reid et al. 1995). Theoretical models thus were needed to remove the effects of effective temperature and surface gravity. We used the PHOENIX model atmospheres (Hauschildt et al. 1999; Allard et al. 2001) to transform EW to the Hα line flux, $F(\mathrm{H}\alpha)$, and then determined the flux ratio $F_{\rm H\alpha}/F_{\rm bol}$ using $F_{\rm bol} = \sigma T^4$. The effective temperature and $\log g$ were adopted from KIC. Finally, the normalized Hα luminosity, $F_{\rm H\alpha}/F_{\rm bol} = L_{\rm H\alpha}/L_{\rm bol}$, was used to signify stellar activity. Figure 3 shows examples of the LAMOST spectra with different strength of Hα emission lines.

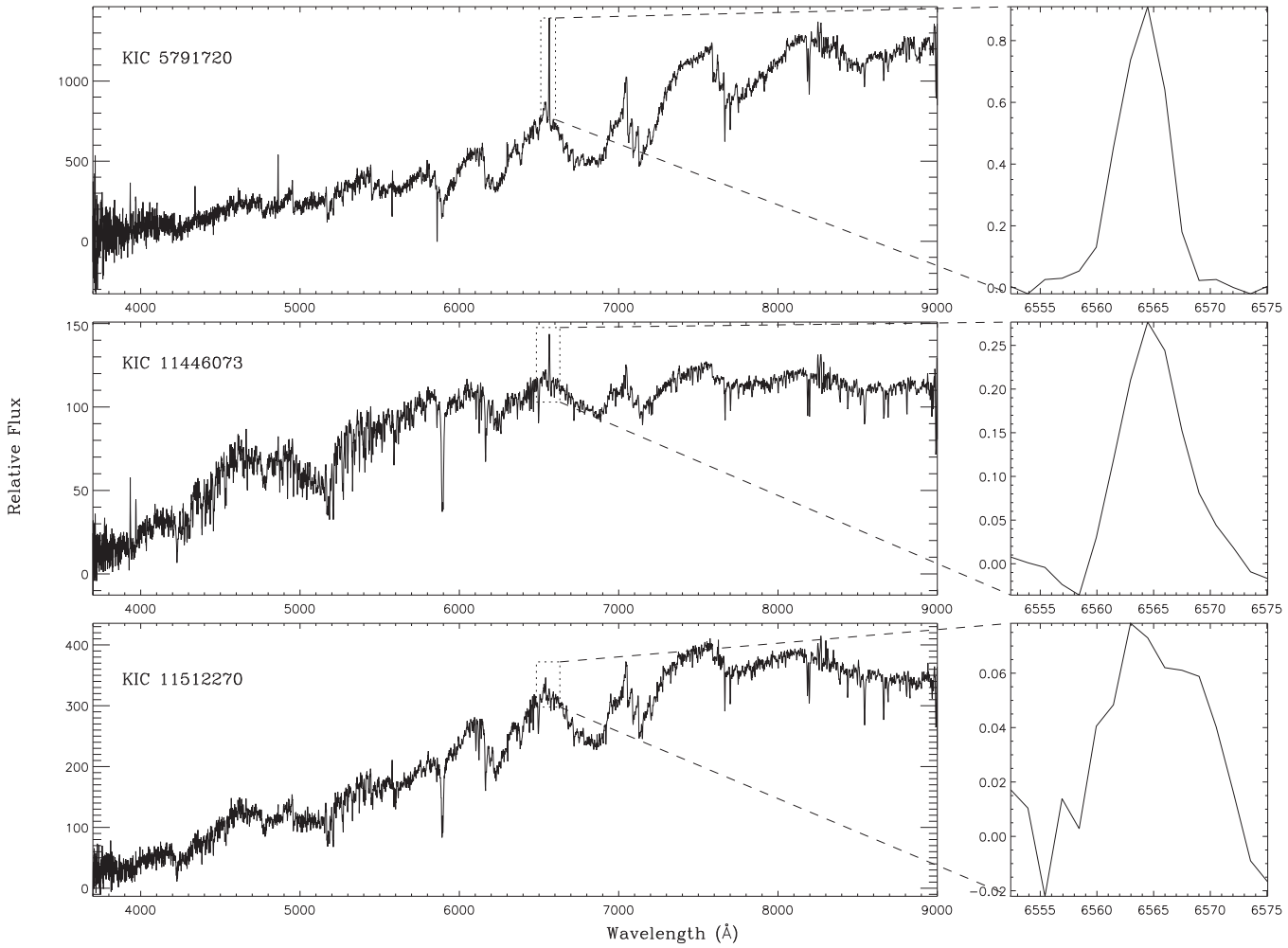

Figure 3. Examples of the LAMOST spectra of the *Kepler* targets. The strongest (top), the intermediate (middle), and the weakest (bottom) Hα emission lines are presented. Left panels show the complete spectral coverage from 3700 to 9000 Å, while the right panels show details of the profiles of the Hα emission line.

Table 1
Parameters of Flaring M Dwarfs

KIC ID	Time (days)	Flare Num.	Period (days)	Amplitude (ppm)	Hα	Hα Activity ($L_{H\alpha}/L_{bol}$)	Flare Activity (L_{flare}/L_{bol})
892376	1415.23	421	1.532[a]	3344	...	...	9.93×10^{-6}
1572802	1415.23	35	0.371[a]	31844	emission	1.813×10^{-4}	1.92×10^{-5}
4355503	982.04	462	5.454[a]	13645	...	...	2.78×10^{-5}
4470937	1067.88	107	...	<200	...	...	1.71×10^{-7}
4726192	1011.29	172	13.799[b]	16644	...	...	6.41×10^{-6}
5016904	1134.84	287	23.81[c]	6294	...	...	1.16×10^{-5}
5597604	1015.27	37	35.259[a]	1847	absorption	...	1.34×10^{-7}

Notes. This table only shows an example format of the parameters for all the 540 flaring M dwarfs: the KIC ID, observational time, number of flares, rotation period, the normalized Hα luminosity, stellar activity, and amplitude of the light curve caused by starspots. The complete table will be available online only. There are 29 flaring stars without apparent rotation periods, and their upper limits of variation amplitude were calculated using the noise of light curves.
[a] Rotation period from McQuillan et al. (2014).
[b] Rotation period from Reinhold et al. (2013).
[c] Rotation period in this work.

(This table is available in its entirety in machine-readable form.)

3. Results

In total, 4664 M dwarfs were retrieved from the *Kepler* archival database, and 103,817 flares were detected in 540 sources over the four-year continuous observations. 540 out of 4664 (~11%) M-type dwarfs are flaring stars. As a comparison, Balona (2015) found 12.75% of cool stars (K and M dwarfs) were flaring stars with $K_p < 12.5$. Walkowicz et al. (2011) found 373 flaring stars out of 23,000 cool dwarfs, of which 2300 were M dwarfs, with an upper detection limit of 16.2%. Davenport (2016) found a detection rate of 2.1% with no cut on

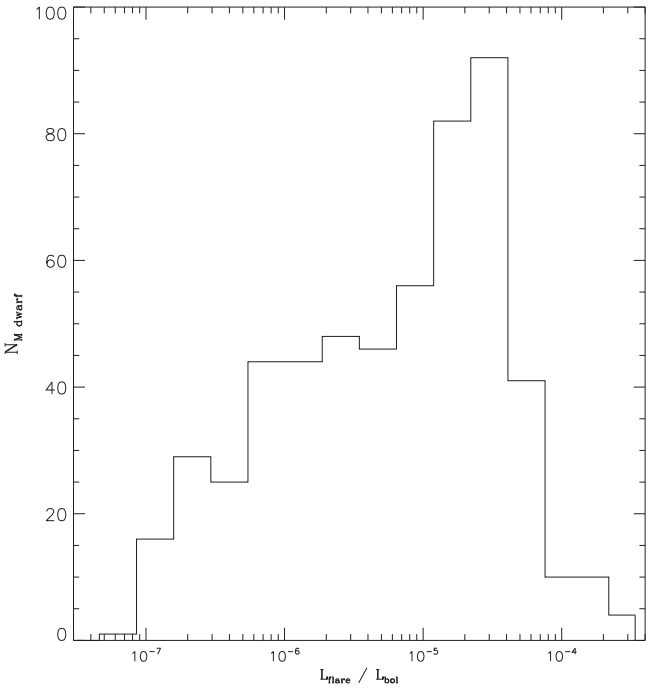

Figure 4. Distribution of the stellar activity of 540 flaring M dwarfs. The activity level ranges from 3.23×10^{-8} to 3.39×10^{-4}.

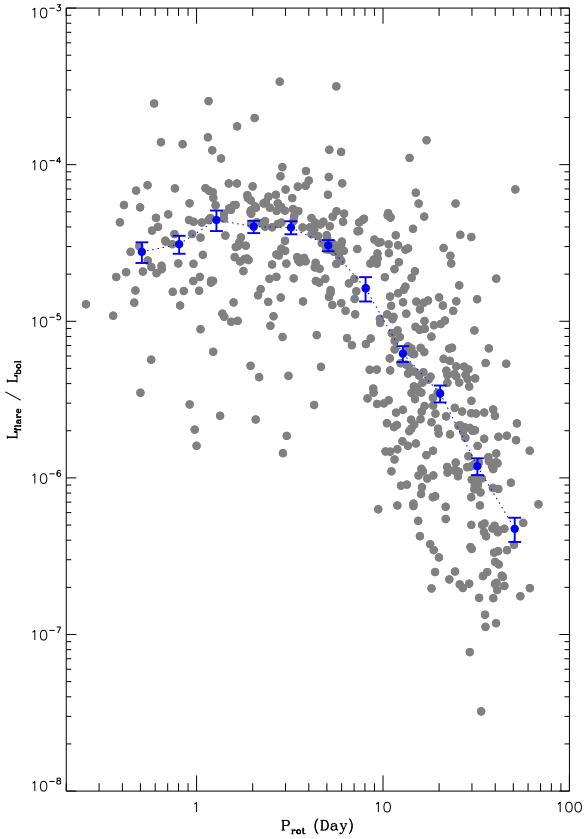

Figure 5. Flare activity vs. rotation period. The blue dots are the median values of evenly divided bins. The scatter of each bin was estimated using the median of absolute deviation (MAD) of the amplitudes, and then multiplied by 1.48 (Mazeh et al. 2015). The error bar on each median value was calculated using $\mathrm{MAD}/\sqrt{n}$, where n is the object number per bin.

$\log g$. Table 1 presents all the flare stars with their KIC ID, duration of observations, detected flare number, rotation period, stellar activity ($L_{\mathrm{H}\alpha}/L_{\mathrm{bol}}$), flare activity ($L_{\mathrm{flare}}/L_{\mathrm{bol}}$), and the amplitude caused by starspots. The beginning and ending dates of a flare, the flare energy, and the event area, as estimated using Equations (1)–(3) are presented for each source.

A total of 133 LAMOST spectra were obtained for 89 flaring M dwarfs. Some of these stars have duplicate observations and the spectra with the highest S/N were used for analysis. 50 of them have the Hα emission line. The normalized Hα luminosity was also calculated based on the LAMOST spectra and the PHOENIX model atmospheres.

3.1. Flare Activity

The energy release of a flare is closely related to stellar activity. As to the emitted energies for our sample, 540 out of 4664 M dwarfs have flares, and the number of flares ranges from several to over 1000 (Table 1). For each star, the flare energy is determined by its total luminosity. Calculation of flare activity was described in Section 2.4. It is a ratio of the flare energy to the total stellar energy. Figure 4 shows the number distribution of the 540 flaring dwarfs. Their activities range from 3.23×10^{-8} to 3.39×10^{-4}, with the majority located between $\sim 1 \times 10^{-5}$ and 5×10^{-5}.

The relation between flare activity ($L_{\mathrm{flare}}/L_{\mathrm{bol}}$) and rotation period is presented in Figure 5. The flare activity first increases as the rotation period decreases, until saturation occurs around a period of four days. The flare activity has a stable value near 4×10^{-4} and slightly declines at $\lesssim 1$ day (Jeffries et al. 2011). This is the dubbed supersaturation phenomenon in the coronal X-ray emission (Wright et al. 2011).

Figure 6 illustrates the relation between flare activity and stellar effective temperature. The lengths of rotation periods are represented by the sizes of data circles. The filled circles are the flaring M dwarfs without any apparent rotation period at the accuracy level of *Kepler*. At stellar temperatures higher than 3200 K (the spectra type near M4), the flare activity is almost stable around 8×10^{-6}. For lower temperatures (<3200 K), the low-activity flaring stars disappear and the average flare activity rapidly increases by nearly one order of magnitude. At the same effective temperature, the stars with shorter rotation periods generally have stronger flare activities. It should be noted that the overall number of targets with temperatures below 3200 K is much smaller than other warmer temperature bins.

Table 2 presents the occurrence of flaring stars. The effective temperatures were evenly binned with a 100 K width. The total numbers of all stars and the stars with flares, and the occurrence rates (in percent) are listed for each temperature bin. The occurrence rate slowly increases as the temperature declines until 3200 K, where the spectral type is close to M4 and the occurrence rate starts to increase. Table 3 is an example showing the format of the flare list.

3.2. Flare Frequency Distribution

The flare frequency distribution (FFD) of M-type stars is shown in Figure 7. In total 103,187 flares were detected for all 540 M-type dwarfs. In the sample of long-period (>10 days) flaring stars, over 30,000 flares were detected. Above the energy of 10^{32} erg, the FFD is well fitted with a power-law, $dN/dE \sim E^{-\alpha}$, where $\alpha \sim 2.07 \pm 0.35$ and the error is the noise level of the line. The two FFDs have very similar slopes, indicating that the period does not affect the FFD.

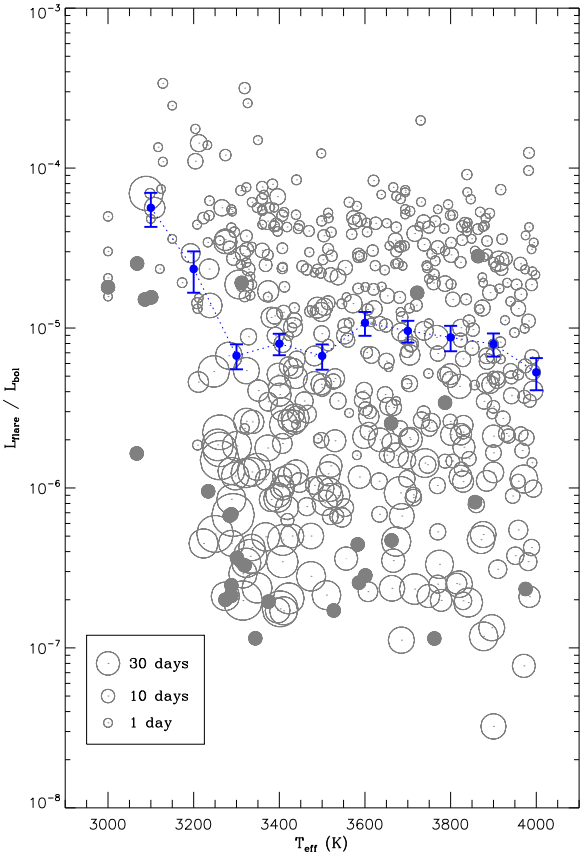

Figure 6. Flare activity vs. stellar effective temperature. Stellar temperatures of our sample have been evenly divided into 11 bins. Blue dots are median values of the bins; the error bars were derived following the same method as in Figure 4. Sizes of the data circles present the lengths of rotation periods. The filled circles are the flaring M dwarfs without any apparent rotation periods at an accuracy level of *Kepler*.

Nearly 1200 flares were detected in 15 M-type dwarfs that have SC observations. Figure 8 shows the FFD of the M dwarfs with SC data, where the detection limits are much lower. Above the energy of 10^{32} erg, the α index of the power law is 2.19 ± 0.33, which is close to the value for the LC data.

As shown in Figure 7, the frequency distribution in the low-energy ($<10^{32}$ erg) region seems to be flat. Hawley et al. (2014) pointed out that the flares were still well detectable at this threshold energy and suggested that the flat distribution at lower energies might be real rather than due to detection limits. However, for the SC data, the FFD is not flat at low energies (Figure 8). Besides, we can estimate the detection limits. The precision of the *Kepler* observations is 100 ppm for a target with $V = 13$, and the boundary condition of flare detection should be at least two data points above 3σ (300 ppm), and thus we calculated the energy detection limit for each source using Equations (1)–(3), and obtained a range of 1.8×10^{29}–1.1×10^{32} erg, which is coincident with where the FFD distribution becomes flat (Figure 7). This indicates that the flat tendency is caused by detection limits.

3.3. Starspots

Along with relative movement and mutual extrusion, the magnetic field that emerges from a starspot's pair could reconnect, resulting in strong energy release, i.e., a flare. Observed amplitudes of the optical brightness modulation imply that a large fraction of the stellar photosphere is covered by cool starspots; thus the starspots are traditionally thought to be a good probe of the magnetic field strengths and flare energies (Berdyugina 2005). For most of the flaring stars, the light-curve variation caused by starspots can be observed with *Kepler* to a high accuracy level when they rotate. The amplitude relative to the quiescent flux could be a proxy for the size of starspots (Candelaresi et al. 2014). However, they are unstable and often shift on the stellar surface, so their amplitudes could vary significantly in each rotation period. In our work, the average amplitudes were presented in Table 1. The method adopted in this work is similar to that of McQuillan et al. (2014), i.e., (1) to fold the light curve with time bins of rotation period in each quarter, (2) to obtain the photometric difference between the 5th and 95th percentiles of normalized flux for all the time bins, and (3) to fit and calculate the average value for all the quarters. The folding and fitting procedures are shown in Figure 9.

Figure 10 shows the correlation between the starspots amplitude and stellar flare activity. The circle size represents the length of rotation period. The blue circles are the upper limit-amplitudes of 29 flaring stars, which do not show apparent rotation periods. The positive correlation between the two parameters is clear, and the long-period M dwarfs generally have lower amplitudes. In Figure 10, the large dispersion at a given flare activity is reasonable due to the following two factors. (i) The inclination angle of the stellar rotation with respect to the observer's line of sight has an impact on the amplitude (Mazeh et al. 2015). If the starspots are temporarily stable on the stellar surface, they will rotate along the latitude near the equator. Consequently, observers can get the maximum light variation from the edge-on view, but from the face-on view, they cannot obtain any light variation caused by starspots. That will result in large dispersion. (ii) Another reason is the instability of starspots. Given that starspots may become stronger, shift or even disappear on the stellar surface, it would cause the amplitude of the light-curve variation to be quite different in each rotation period. Therefore, a highly active star with larger amplitude could be affected more significantly and thus exhibit large dispersion, as shown in Figure 10.

3.4. Hα Activity

The Hα emission line is thought to be strongly affected by the magnetic field and rotation period, both of which are key to the flare mechanism. Therefore, it is a useful proxy for studying the magnetic field and stellar activity (Reiners 2012). In our sample, there are 89 M-type flaring dwarfs, whose spectra are available from the LAMOST DR4. Among these flaring dwarfs, 50 have Hα emission and their normalized Hα luminosities were calculated and presented in Table 1.

It will also be interesting to check the relation between the normalized Hα luminosity ($L_{H\alpha}/L_{bol}$) and flare activity because this parameter is also a proxy for stellar activity. Figure 11 shows a generally power-law dependence of $L_{H\alpha}/L_{bol}$ on the flare activity, $L_{H\alpha}/L_{bol} = (L_{flare}/L_{bol})^a + 10^b$, where $a \sim 0.44 \pm 0.03$ and $b \sim -2.03 \pm 0.11$. The stellar periods of variation range from 0.35 to 54.53 days, which is indicated by the sizes of open data circles. Two targets, KIC 9222296 and KIC 11925804, do not show any apparent periods, and are represented by filled circles. The long-period stars have low $L_{H\alpha}/L_{bol}$ ratios on average; there

Table 2
The Relation between Flaring Star Incidence Rate and Effective Temperature

Temperature (K)	3000–3100	3100–3200	3200–3300	3300–3400	3400–3500	3500–3600	3600–3700	3700–3800	3800–3900	3900–4000
Total star number	22	44	213	371	439	475	630	760	672	1038
Flaring star number	10	12	47	72	72	56	73	59	69	70
Flaring star rate	45.5%	27.3%	22.1%	19.4%	16.4%	11.8%	11.5%	7.8%	10.3%	6.7%
Mean flare activity (10^{-5})	3.15	9.43	3.10	3.21	1.45	1.60	1.98	1.99	1.97	1.43

Note. Effective temperatures were binned by 100 K; the occurrence rates (in %) of flaring stars; the averaged flare activity of each temperature bin.

Table 3
Flare Parameters

KIC ID	Begin Time (Day)	End Time (Day)	Energy[a] (erg)	Flare Area[b]
5966921	214.45	214.82	35.82	2.37×10^{-3}
5966921	656.12	656.43	35.32	9.16×10^{-4}
7341653	1237.15	1237.32	33.77	6.51×10^{-4}
5858361	153.40	153.68	33.16	1.97×10^{-5}
5791720	886.96	887.07	34.84	1.05×10^{-3}
5791720	903.13	903.25	34.38	3.06×10^{-4}

Notes.
[a] Energy in logarithm.
[b] In proportion to the surface area of a star.

(This table is available in its entirety in machine-readable form.)

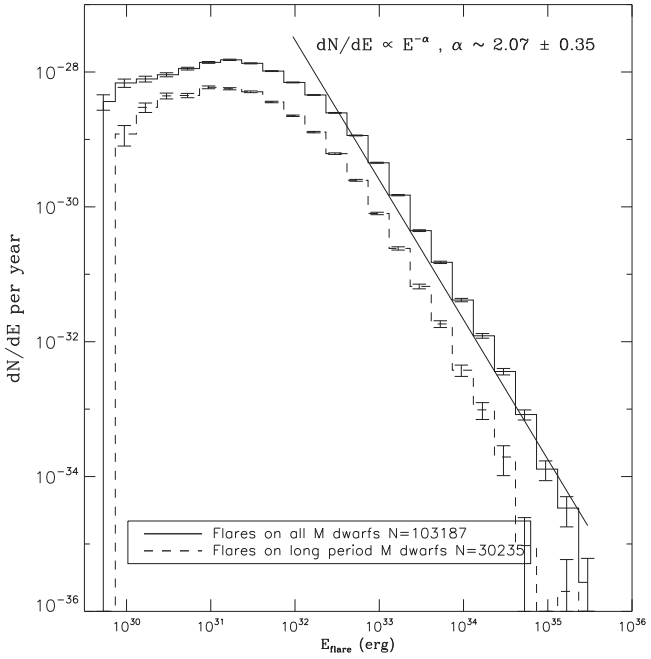

Figure 7. Frequency distribution of flares in M-type dwarfs. Note the frequencies have been divided by the bin width. The solid straight line is a power-law fit with an index of ∼2.07. The dashed line represents the long-period (>10 days) flaring stars. Error bars of each energy bin were estimated using a square root of the number of flares in each bin.

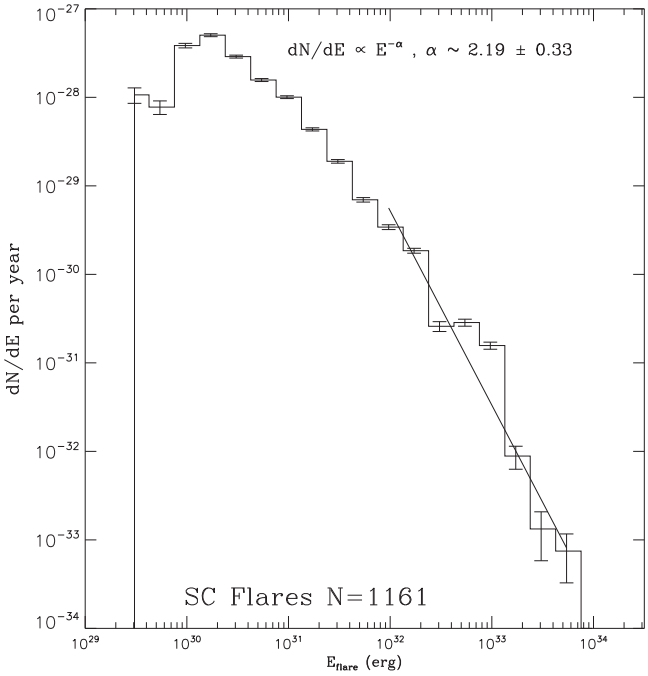

Figure 8. Same as Figure 7 but for the SC data.

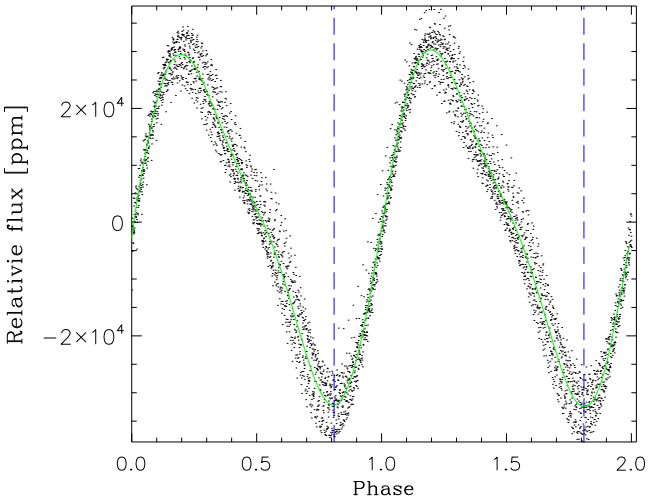

Figure 9. Folded light curve in one-quarter phase with a binning of two rotation periods. The green line is a fit to the data, and the section between the two blue dashed lines is used to define the amplitude of stellar flare.

are also short-period stars with low $L_{H\alpha}/L_{bol}$ such as KIC 12688403 ($<4 \times 10^{-4}$), whose period is 3.045 day. It implies that the flare activity might be even better correlated with rotation period than chromospheric activity. KIC 11512270 with 39 detected flares shows the weakest stellar activity, $L_{flare}/L_{bol} = 6.6 \times 10^{-7}$, among all the active stars with Hα emission. The active level of KIC 11512270 is also the lowest in the flare activity distribution. This indicates that the low-activity star also can produce Hα emission. Given that the dispersion of the data is relatively small and most of the spectroscopic observations are one to two years later than *Kepler*, this implies that the magnetic filed and the energy release mechanism on these stars are probably stable on a timescale of years.

4. Discussion

4.1. Flare Activity

According to the dynamo theory, the interaction between stellar rotation and convection generates magnetic fields (Parker 1979), and rotation period is an indicator of stellar chromospheric activity. Moreover, the effects of these two parameters on the efficiency of magnetic dynamo have been combined into a single parameter, the Rossby number, by Noyes et al. (1984). Recently, a series of papers studied the relation between stellar activity and rotation period and/or the Rossby number (Pizzolato et al. 2003; Marsden et al. 2009; Wright et al. 2011; Douglas et al. 2014; West et al. 2015; Argiroffi et al. 2016; Davenport 2016; Guinan et al. 2016; Suárez Mascareño et al. 2017). In the observations of coronal X-ray emission, the stellar activity-period relation can be

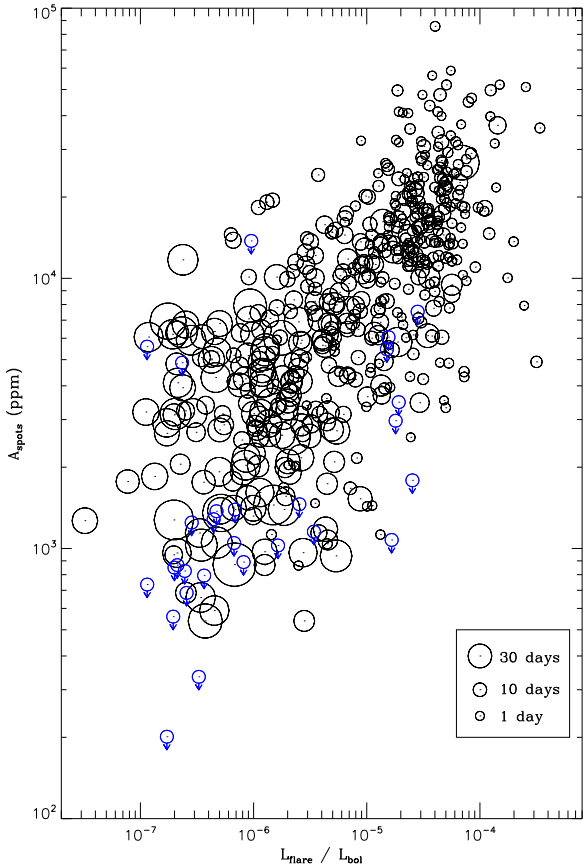

Figure 10. General positive correlation between the starspot's amplitude and stellar flare activity. The size of the circle represents the length of rotation period. There are 29 flaring stars without apparent rotational periods. Their upper limit of spot amplitude is calculated by the noise of light curves and plotted as blue circles.

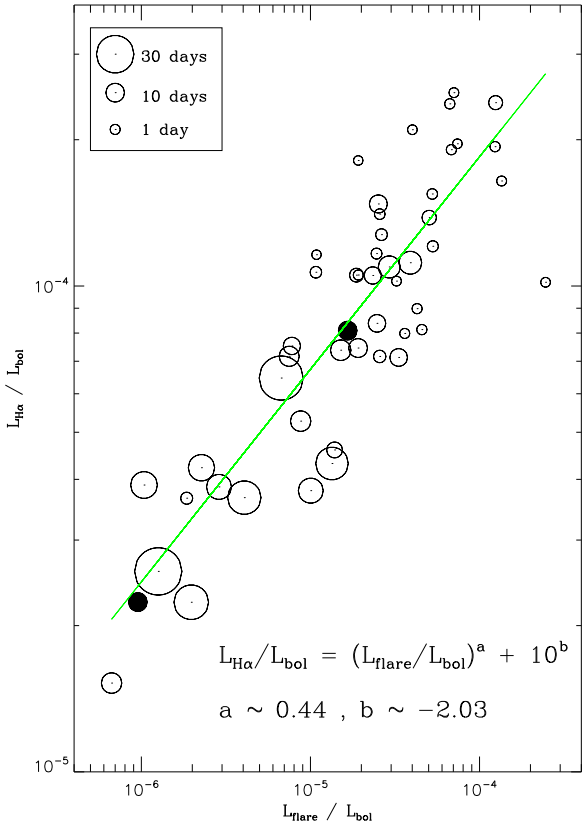

Figure 11. Relation between normalized Hα luminosity and the flare activity. The size of the open circle represents the period length, while two stars without apparent periods are represented by filled circles.

described as three phases. (1) The stellar activity has a negative power-law dependence on rotation period at the periods $\gtrsim$5 days, although the slope of this power law is under debate. (2) Between the period of one and five days, the stellar activity shows a saturated state with $L_X/L_{bol} \sim 10^{-3}$. (3) For the very fast rotations with periods of less than one day, the stellar activity has been observed to decrease below the saturation level. This phenomenon is dubbed as "supersaturation," of which the true nature is also under debate.

Alternatively, for the indicators of chromospheric emission such as Ca II and Hα lines, the saturation value is $L_{H\alpha}/L_{bol} \sim 10^{-4}$, which is lower than X-ray emission by one order of magnitude. Moreover, the chromospheric emission indicators do not show any evidence of supersaturation (Marsden et al. 2009; Christian et al. 2011). As shown in Figure 5, the flare activity has a negative power-law dependence on rotation period at periods of >5 days. It then reaches a saturation state with $\sim 5 \times 10^{-5}$. Finally, the supersaturation is obviously less than one day. All of these tendencies are similar with previous studies on X-ray emission (e.g., Wright et al. 2011; Argiroffi et al. 2016). As flare energy mainly comes from the photosphere, these results indicate the coherence in energy release between corona and photosphere.

In our sample, there are 89 M-type flaring stars with LAMOST spectra, and 50 (55%) of them have the Hα emission, which displays a good power-law relation with flare activity, i.e., $L_{H\alpha}/L_{bol} \sim (L_{flare}/L_{bol})^a$, where $a \sim 0.44$. On the other hand, the flare activity is proportional to the square of the normalized Hα luminosity. Based on this relation, the small enhancement in chromosphere activity may cause a huge rise in flare energy, which suggests that the superflares or hyperflares may not need any extra mechanism to explain such as tidal interaction, or inter-connection with other objects (Aschwanden et al. 2000; Karoff et al. 2016).

It should be noted that nearly half of the flaring M dwarfs lack the Hα emission, despite having many flares detected. Figure 12 shows the relation between flare activity and rotation period for all those stars with the LAMOST spectra available. There are two exceptions, KIC 9222296 and KIC 11925804, which do not exhibit any apparent period. The active stars have relatively short periods and high activity levels, and all the stars with rotation periods shorter than 10 days show emission lines, which implies that all the fast rotating stars have strong and stable magnetic fields.

However, above the rotation period of 10 days, the active stars are mixed with inactive ones; this mixing is quite obvious near the flare activity of 10^{-6}. This may be explained by this mechanism: when magnetic reconnection occurs, the higher energy levels of hydrogen are thermalized due to collisions within photosphere and chromosphere, and tends to return to lower states after the reconnection. If the plasma recovery timescale is shorter than the average flare interval, the Hα absorption line could be observed in quiescent time. Apparently, the inactive stars do not have frequent magnetic reconnection or a short recovery timescale, which indicates that the reconnection occurs in denser plasma regions.

Figure 12 shows that the boundary between the active and inactive stars is nearly 10 days in period, or 6×10^{-6} in flare activity. Near this region, there is slight mixing of the active and inactive stars. If this boundary is actually 10 days, the mechanism of flares should be investigated. In Figure 7, the FFD of long-period (>10 days) stars are similar to that of the total sample, although rapid rotation may cause strong magnetic activity. The occurrence rate of superflares can be inferred from the FFD. Including more superflares could make the slope of FFD flat. On the other hand, the similarity in slope suggests that the rotational period does not affect the occurrence of superflares, or that the generation of superflares might not be affected by one single mechanism only (such as the chromospheric activity).

4.2. Active Fraction

M-type dwarfs encompass many important regions in stellar parameter space including the onset of complete convection in the stellar interior, which occurs near the spectral type M4. Table 2 presents the number fraction of flaring stars (hereafter, flare fraction or active fraction) in each subtype. Generally, the flaring fraction increases sightly in the early subtypes and rises sharply near M4.

West et al. (2004) presented a spectroscopic analysis of nearly 8000 late-type dwarfs in the Sloan Digital Sky Survey, using Hα as an activity indicator. In their sample, 5789 M-type dwarfs are between the spectral type M1 and M5, corresponding to the effective temperatures from 4000 to 3000 K. They gave the active fraction using the Hα emission (hereafter, emission fraction) and found a similar tendency. A comparison between the flaring fraction and the emission fraction is presented in Figure 13. The reason that some flaring stars do not have Hα emission has been discussed in Section 4.1, which also explains why the flare fraction is higher than the emission fraction in early subtypes. Moreover, the average flare activity is low in the early subtypes (Table 2). In the intermediate subtypes, the stellar activity becomes strong, resulting in Hα emission in almost all the flaring stars and consequently similar active fractions.

As shown in Figures 13 and 14, flare activity has similar behaviors to other indicators. Moreover, Flare activity quantifies the released stellar energy. It is a more suitable indicator for stellar activity than any emission line or rotation period, especially in the boundary region.

4.3. Supersaturation

The supersaturation effect was first observed in X-ray activity (Randich et al. 1996). The clues of supersaturation in M dwarfs were then reported through X-ray observations (James et al. 2000). Argiroffi et al. (2016) found that supersaturation is better described by rotation period than the Rossby number. Which of the two theories is responsible for the mechanism of supersaturation is still under debate today.

One is the centrifugal stripping proposed by Jardine & Unruh (1999). This theory argues that as the corotation radius of a rapidly rotating star becomes very close to stellar surface, the volume outside the corotation radius decreases; this is an important factor for stable coronal structure. As a result, the luminosity of coronal X-ray emission decreases.

The other mechanism is the polar up-drift migration proposed by Stepień et al. (2001). This theory assumes that

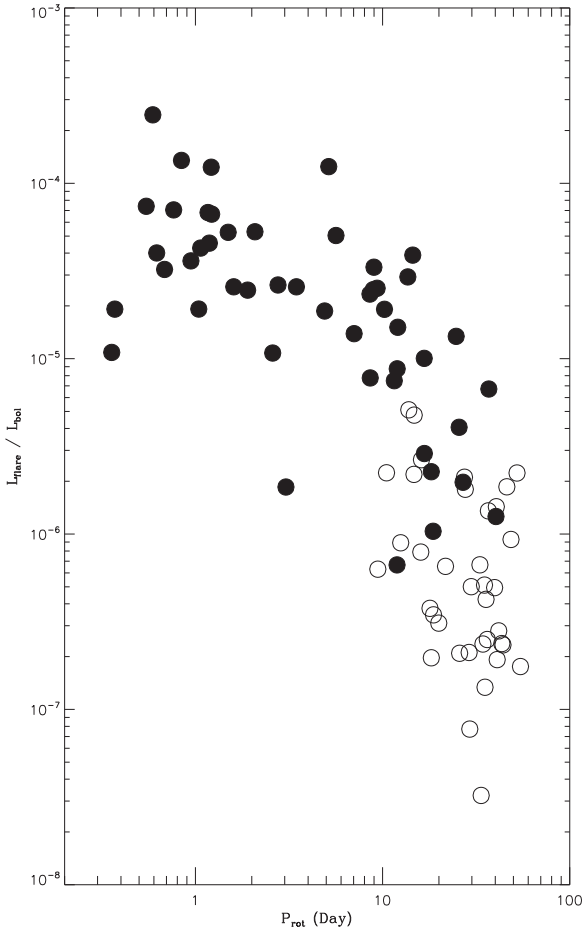

Figure 12. Relation between rotation period and flare activity of the stars with LAMOST spectra. The filled circles represent the stars with Hα emission, while the stars that have absorption lines are represented by open circles.

the polar up-drift migration is caused by the nonuniform heating that characterizes the base of the convective envelope. It explains that at high rotation velocities, active regions preferentially concentrate near the stellar poles and coronal plasma. It thus reduces the filling factor and, subsequently, decreases the X-ray emission.

The fundamental difference between these two theories is in the underlying structure of coronal loops that give rise to X-ray emission. Moreover, if coronal supersaturation were caused by the migration of active regions toward the poles, one might expect to see supersaturation in chromospheric emission as well. A series of papers have studied the chromosphere supersaturation in a sample of F-, G-, K-, and M-type stars but found no evidence for a decline in the chromospheric activity (Marsden et al. 2009; Jackson & Jeffries 2010; Argiroffi et al. 2016).

Figure 14 shows the relation between rotation period and normalized Hα luminosity, which is the indicator of chromospheric activity. It can be inferred from this figure that there is no evidence for the existence of the supersaturation region, which is consistent with previous studies (Marsden et al. 2009; Christian et al. 2011; Argiroffi et al. 2016).

Besides, if the active regions migrate toward the poles, the light-curve variation caused by starspots, which formed on the photosphere, should consequently reduce. Figure 15 shows the relation of their amplitudes with rotation period. Due to the

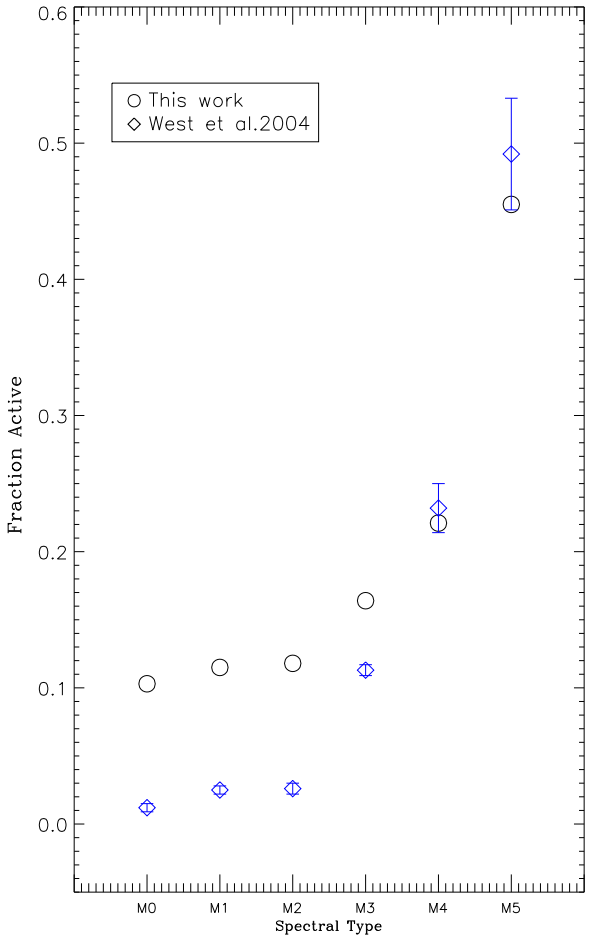

Figure 13. Active fraction vs. spectral type. The open circles were calculated from the data in Table 2. The diamonds are adopted from (West et al. 2004, Figure 1 therein).

inclination angles, there are a few outliers below 10 days whose amplitudes are apparently lower than 10,000 ppm, but the saturation region can be seen at periods of <5 days. No decrease in the amplitude is found in short-period objects, which implies that there is no apparent migration toward the poles. As a result, our study probably prefers the theory of centrifugal stripping.

4.4. Magnetic Field of the M Flaring Star

Most of our current knowledge about magnetic fields on cool stars and in starspots is based on the measurements of Zeeman broadening, which reveal the distribution of magnetic field strengths with little dependence on field geometry, which is unknown for most cases (Robinson 1980; Saar et al. 1986; Valenti & Johns-Krull 2001). The size of the starspots that reveal the magnetic filed (Berdyugina 2005) has a good positive correlation with stellar activity (Figure 10), indicating that the stellar activity is mainly determined by the magnetic filed. Most of the flare energy is due to the release of magnetic energy (e.g., Sun et al. 2012), which can be estimated from the field strength within a certain volume V:

$$E = \int_V \frac{B^2}{8\pi} dV. \quad (5)$$

Assuming that the magnetic field strength is uniform and $V = L^3$, where L is the size of the active region (Balona 2015),

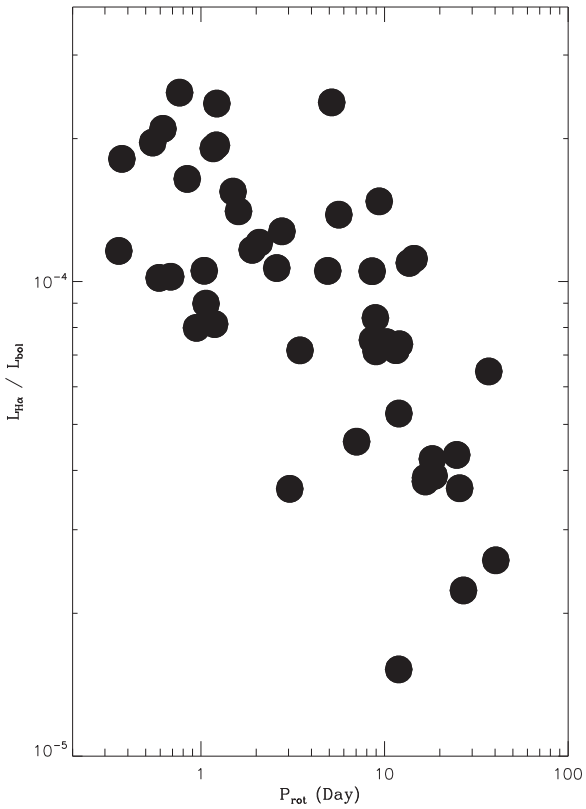

Figure 14. Relation between rotational period and normalized Hα luminosity.

Equation 5 can be simplified into $E = L^3B^2/8\pi$. We can estimate a range of the magnetic field strength from several hundred Gauss to ~100 k Gauss using the flare energy. Reiners et al. (2012) did statistical studies of 93 M-type dwarfs, and found that their average magnetic field strength is several kilogauss. Our result is thus reasonable and implies that the superflares do not have very strong magnetic fields.

Among the 540 flaring M dwarfs, McQuillan et al. (2014) and Reinhold et al. (2013) derived rotation periods for 421 of them, and another 90 were measured in this work using the light-curve variation caused by starspots rotation. There are 29 stars that do not show any apparent period. The reason may be threefold: (i) the inclination angle and low-activity level lead to the small amplitude of the light curve at the accuracy level of *Kepler*; (ii) their rotation periods are so long that they exceed one quarter (90 days), resulting in low visibility in the frequency spectrogram; and (iii) there are polar spots on fast rotating stars (Schüssler & Solanki 1992), and the light variation cannot be seen through rotation. However, it is interesting to find that some of them show many superflares and display a high level of activity. This phenomenon will be explored in a future paper.

5. Summary

We present 540 flaring M dwarfs in the *Kepler* fields with 103,187 flares detected using the *Kepler* long-cadence (LC) data. Their energies are estimated, and the normalized flare activities, $L_{\rm flare}/L_{\rm bol}$, are measured for each star. Through analysis, we find that this parameter is a good indicator for

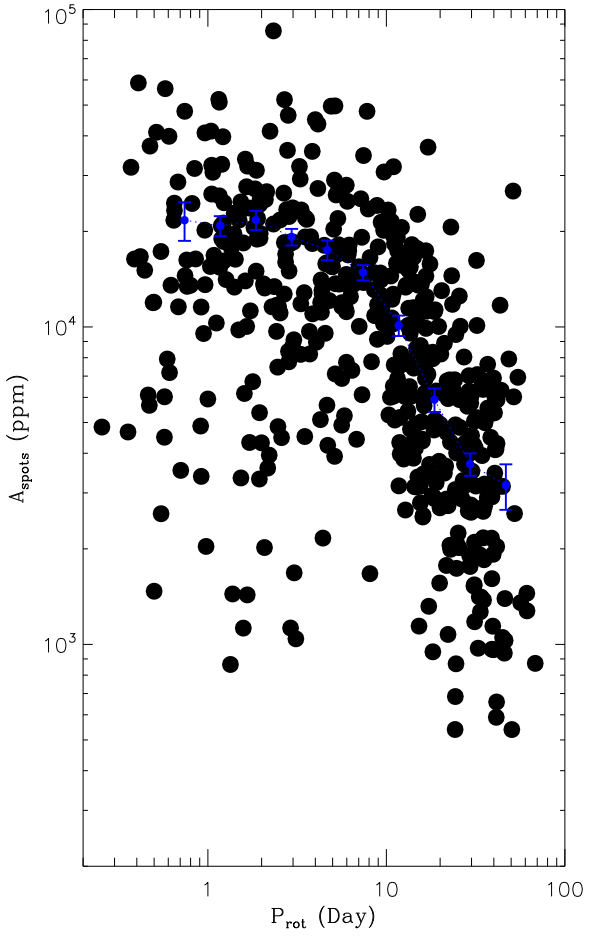

Figure 15. Relation between rotation period and amplitude of starspots. The periods are binned into 10 sections, and the average amplitude (blue filled circle) is calculated for each bin, along with the error bar. Outliers are excluded in the calculations of the average values.

stellar activity. Its relation with other stellar parameters is summarized as follows.

(1) The $L_{\rm flare}/L_{\rm bol}$ versus $P_{\rm rot}$ relation is rather similar to $L_{\rm X}/L_{\rm bol}$ versus $P_{\rm rot}$ in that there are also three phases: supersaturation, saturation, and exponential decay, corresponding to the ultra-short period, short period, and long period.

(2) The flare activity and the flare fraction in M dwarfs show a steep rise near spectral type M4, which is consistent with the prediction of turbulent dynamo. The flare fraction is higher than the emission fraction in early subtypes, and these two fractions become similar in the intermediate subtype.

(3) The size of starspots is positively correlated with the flare activity. However, this relation largely depends on the inclination angle.

(4) There is a power-law dependence of flare activity on the indicator of chromospheric emission, $L_{\rm H\alpha}/L_{\rm bol} \sim (L_{\rm flare}/L_{\rm bol})^a$, where $a \sim 0.44$. This relation is important because it reflects the correlation between chromospheric activity and energy release from the photosphere. Based on this relation, the small enhancement in chromospheric activity may cause a huge rise in flare energy, indicating that the superflares or hyperflares may not need an extra mechanism to generate (Shibayama et al. 2013; Davenport 2016).

A period of 10 days or a flare activity level of 6×10^{-6} could be a boundary between the active and inactive stars. Above this boundary, all the flaring M dwarfs have Hα emission. Flares are also detected in the inactive stars, which could be explained by the long flare interval or short recovery timescale.

The relation between rotation period and the normalized Hα luminosity, as well as the size of starspots, shows no evidence of supersaturation, suggesting that the theory of centrifugal stripping could be at work.

The FFD has a power-law distribution, $dN/dE \sim {\rm E}^{-\alpha}$ ($\alpha \sim 2.07 \pm 0.35$). The long- and short-period stars show a similar slope in distribution, indicating that the superflares have the same mechanism.

It should be noted that, because our flare samples are incomplete, the error bars in these figures are based on the samples of unknown completeness and therefore have undefined reliability.

We sincerely thank the anonymous referee for very helpful constructive comments and suggestions, which have significantly improved this article. We acknowledge support from the Chinese Academy of Sciences (grant XDB09000000), from the 973 Program (grant 2014CB845705), and from the National Science Foundation of China (grants NSFC-11333004/11425313). The paper includes data collected by the *Kepler* mission. Funding for the *Kepler* mission is provided by the NASA Science Mission Directorate. All the data presented in this paper were obtained from the Mikulsk Archive for Space Telescopes (MAST) at STScI, which is operated by the Association of Universities for Research in Astronomy, Inc., under NASA contract NAS5-26555. Support for MAST for non-HST data is provided by the NASA Office of Space Science via grant NNX09AF08G and by other grants and contracts. Guoshoujing Telescope (the Large Sky Area Multi-Object Fiber Spectroscopic Telescope LAMOST) is a National Major Scientific Project built by the Chinese Academy of Sciences. Funding for the project has been provided by the National Development and Reform Commission. LAMOST is operated and managed by the National Astronomical Observatories, Chinese Academy of Sciences. The LAMOST FELLOWSHIP is supported by Special Funding for Advanced Users, budgeted and administrated by Center for Astronomical Mega-Science, Chinese Academy of Sciences (CAMS).

Appendix

For interested parties, data tables of all the Kepler M dwarves that have flares are available in individual .tar.gz packages at Zenodo Yang (2017). The DOI for the data is [10.5281/zenodo.897031]. Each quarter has a individual table, and the table includes 4 columns: BKJD, relative flux, fitted line, and flare flux.

ORCID iDs

Huiqin Yang https://orcid.org/0000-0003-4917-7221
Jifeng Liu https://orcid.org/0000-0002-2874-2706
Xuan Fang https://orcid.org/0000-0002-3981-7355

References

Akeson, R. L., Chen, X., Ciardi, D., et al. 2013, PASP, 125, 989
Allard, F., Hauschildt, P. H., Alexander, D. R., Tamani, A., & Schweitzer, A. 2001, ApJ, 556, 357

Argiroffi, C., Caramazza, M., Micela, G., et al. 2016, A&A, 589, A113
Aschwanden, M. J., Tarbell, T. D., Nightingale, R. W., et al. 2000, ApJ, 535, 1047
Balona, L. A. 2012, MNRAS, 423, 3420
Balona, L. A. 2012, MNRAS, 447, 2714
Batalha, N. M., Rowe, J. F., Bryson, S. T., et al. 2013, ApJS, 204, 24
Benz, A. O., & Güdel, M. 2010, ARA&A, 48, 241
Berdyugina, S. V. 2005, LRSP, 2, 8
Borucki, W. J., Koch, D., Basri, G., et al. 2010, Sci, 327, 977
Brown, T. M., Latham, D. W., Everett, M. E., & Esquerdo, G. A. 2011, AJ, 142, 112
Bryson, S. T., Jenkins, J. M., Gilliland, R. L., et al. 2013, PASP, 125, 889
Bryson, S. T., Jenkins, J. M., Klaus, T. C., et al. 2010, Proc. SPIE, 7740, 77401D
Candelaresi, S., Hillier, A., Maehara, H., Brandenburg, A., & Shibata, K. 2014, ApJ, 792, 67
Chang, H.-Y., Song, Y.-H., Luo, A.-L., et al. 2017, ApJ, 834, 92
Christian, D. J., Mathioudakis, M., Arias, T., Jardine, M., & Jess, D. B. 2011, ApJ, 738, 164
Coughlin, J. L., Mullally, F., Thompson, S. E., et al. 2016, ApJS, 224, 12
Cui, X., Zhao, Y. H., Chu, Y. Q., et al. 2012, RAA, 12, 1197
Davenport, J. R. A. 2016, ApJ, 829, 23
De Cat, P., Fu, J. N., Ren, A. B., et al. 2015, ApJS, 220, 19
Donati, J.-F., Morin, J., Petit, P., et al. 2008, MNRAS, 390, 545
Douglas, S. T., Ageros, M. A., Covey, K. R., et al. 2014, ApJ, 795, 161
Dressing, C. D., & Charbonneau, D. 2013, ApJ, 767, 95
Everett, M. E., Howell, S. B., Silva, D. R., & Szkody, P. 2013, ApJ, 771, 107
Faigler, S., Tal-Or, L., Mazeh, T., Latham, D. W., & Buchhave, L. A. 2013, ApJ, 771, 26
Gao, Q., Xin, Y., & Liu, J.-F. 2016, ApJS, 224, 37
Guinan, E. F., Engle, S. G., & Durbin, A. 2016, ApJ, 821, 81
Hauschildt, P. H., Allard, F., & Baron, E. 1999, ApJ, 512, 377
Hawley, S. L., Davenport, J. R. A., Kowalski, A. F., et al. 2014, ApJ, 797, 121
Hilton, E. J. 2011, PhD thesis, Univ. Washington
Huber, D. 2014, Kepler Stellar Properties Catalog Update for Q1-Q17 Transit Search (KSCI-19083), http://exoplanetarchive.ipac.caltech.edu/docs/KeplerStellar_Q1_17_documentation.pdf
Huber, D., Silva Aguirre, V., Matthews, J. M., et al. 2014, ApJS, 211, 2
Ip, W.-H., Kopp, A., & Hu, J.-H. 2004, ApJL, 602, L53
Jackson, R. J., & Jeffries, R. D. 2010, MNRAS, 407, 465
James, D. J., Jardine, M. M., Jeffries, R. D., et al. 2000, MNRAS, 318, 1217
Jardine, M., & Unruh, Y. C. 1999, A&A, 346, 883
Jeffries, R. D., Jackson, R. J., Briggs, K. R., Evans, P. A., & Pye, J. P. 2011, MNRAS, 411, 2099
Karoff, C., Knudsen, M. F., De Cat, P., et al. 2016, NatCo, 7, 11058
Koch, D. G., Borucki, W. J., Basri, G., et al. 2010, ApJL, 713, L79
Kowalski, A. F., Hawley, S. L., Holtzman, J. A., Wisniewski, J. P., & Hilton, E. J. 2010, ApJL, 714, L98
Kowalski, A. F., Hawley, S. L., Wisniewski, J. P., et al. 2013, ApJS, 207, 15
Kretzschmar, M. 2011, A&A, 530, A84
Lurie, J. C., Davenport, J. R. A., Hawley, S. L., et al. 2015, ApJ, 800, 95
Maehara, H., Shibayama, T., Notsu, S., et al. 2012, Natur, 485, 478
Marsden, S. C., Carter, B. D., & Donati, J.-F. 2009, MNRAS, 399, 888
Mathur, S. 2016, Kepler Stellar Properties Catalog Update for Q1-Q17 DR25 Transit Search (KSCI-19097-003), http://exoplanetarchive.ipac.caltech.edu/docs/KSCI-19097-003.pdf
Mazeh, T., Perets, H. B., McQuillan, A., & Goldstein, E. S. 2015, ApJ, 801, 3
McQuillan, A., Mazeh, T., & Aigrain, S. 2014, ApJS, 211, 24
Mochnacki, S. W., & Zirin, H. 1980, ApJL, 239, L27
Morin, J., Donati, J.-F., Petit, P., et al. 2008, MNRAS, 390, 567
Noyes, R. W., Hartmann, L. W., Baliunas, S. L., Duncan, D. K., & Vaughan, A. H. 1984, ApJ, 279, 763
Osten, R. A., Kowalski, A., Sahu, K., & Hawley, S. L. 2012, ApJ, 754, 4
Parker, E. N. 1979, Cosmical Magnetic Fields: Their Origin and Their Activity (Oxford: Oxford Univ. Press), 532
Pizzolato, N., Maggio, A., Micela, G., Sciortino, S., & Ventura, P. 2003, A&A, 397, 147
Press, W. H., Teukolsky, S. A., Vetterling, W. T., & Flannery, B. P. 1992, Numerical Recipes in C. The art of Scientific Computing (2nd ed.; Cambridge: Cambridge Univ. Press)
Randich, S., Schmitt, J. H. M. M., Prosser, C. F., & Stauffer, J. R. 1996, A&A, 305, 785
Reid, I. N., Hawley, S. L., & Gizis, J. E. 1995, AJ, 110, 1838
Reiners, A. 2012, LRSP, 9, 1
Reiners, A., & Basri, G. 2009, A&A, 496, 787
Reiners, A., Joshi, N., & Goldman, B. 2012, AJ, 143, 93
Reinhold, T., Reiners, A., & Basri, G. 2013, A&A, 560, A4
Robinson, R. D., Jr 1980, ApJ, 239, 961
Rubenstein, E. P., & Schaefer, B. E. 2000, ApJ, 529, 1031
Saar, S. H., Linsky, J. L., & Beckers, J. M. 1986, ApJ, 302, 777
Schüssler, M., & Solanki, S. K. 1992, A&A, 264, L13
Shibayama, T., Maehara, H., Notsu, S., et al. 2013, ApJS, 209, 5
Shimizu, T. 1995, PASJ, 47, 251
Simon, T., Linsky, J. L., & Schiffer, F. H., III 1980, ApJ, 239, 911
Stepień, K., Schmitt, J. H. M. M., & Voges, W. 2001, A&A, 370, 157
Su, D.-Q., Cui, X.-Q., Wang, Y., & Yao, Z. 1998, Proc. SPIE, 3352, 76
Suárez Mascareño, A., Rebolo, R., González Hernández, J. I., & Esposito, M. 2017, MNRAS, 468, 4772
Sun, X., Hoeksema, J. T., Liu, Y., et al. 2012, ApJ, 748, 77
Valenti, J. A., & Johns-Krull, C. M. 2001, in ASP Conf. Ser. 248, Magnetic Fields across the Hertzsprung-Russell Diagram, ed. G. Mathys et al. (San Francisco, CA: ASP), 179
Van Cleve, J. E., & Caldwell, D. A. 2009, Kepler Instrument Handbook, KSCI-19033, https://archive.stsci.edu/kepler/manuals/KSCI-19033-001.pdf
Verner, G. A., Elsworth, Y., Chaplin, W. J., et al. 2011, MNRAS, 415, 3539
Vilhu, O. 1984, A&A, 133, 117
Walkowicz, L. M., Basri, G., Batalha, N., et al. 2011, AJ, 141, 50
West, A. A., Hawley, S. L., Walkowicz, L. M., et al. 2004, AJ, 128, 426
West, A. A., Weisenburger, K. L., Irwin, J., et al. 2015, ApJ, 812, 3
Wright, N. J., Drake, J. J., Mamajek, E. E., & Henry, G. W. 2011, ApJ, 743, 48
Yang, H. 2017, The Flaring Activity of M Type Dwarfs In Kepler Feild, Zenodo, doi:10.5281/zenodo.897031